

Towards Generalization of Graph Neural Networks for AC Optimal Power Flow

Olayiwola Arowolo

Department of Electrical Sustainable Energy
Delft University of Technology
Delft, the Netherlands
o.a.arowolo@tudelft.nl

Jochen. L Cremer

Department of Electrical Sustainable Energy
Delft University of Technology
Delft, the Netherlands
j.l.cremer@tudelft.nl

Abstract—AC Optimal Power Flow (ACOPF) is computationally expensive for large-scale power systems, with conventional solvers requiring prohibitive solution times. Machine learning approaches offer computational speedups but struggle with scalability and topology adaptability without expensive retraining. To enable scalability across grid sizes and adaptability to topology changes, we propose a Hybrid Heterogeneous Message Passing Neural Network (HH-MPNN). HH-MPNN models buses, generators, loads, shunts, transmission lines and transformers as distinct node or edge types, combined with a scalable transformer model for handling long-range dependencies. On grids from 14 to 2,000 buses, HH-MPNN achieves $<1\%$ optimality gap on default topologies. Applied zero-shot to thousands of unseen topologies, HH-MPNN achieves $<3\%$ optimality gap despite training only on default topologies. Pre-training on smaller grids also improves results on a larger grid. Computational speedups reach $1,000\times$ to $10,000\times$ compared to interior point solvers. These results advance practical, generalizable machine learning for real-time power system operations.

Index Terms—Graph Neural Network, Generalization, Machine Learning, Optimal Power Flow, Topology

I. INTRODUCTION

The AC optimal power flow (ACOPF) problem determines the optimal generator dispatch in a grid, subject to physical and engineering constraints [1]. Despite being fundamental to power systems operations, including unit commitment and transmission expansion planning [2], ACOPF remains computationally challenging for large grids due to its non-convexity and non-linearity. No commercial solver guarantees globally optimal solutions for large grids within acceptable timeframes [1]. With system operators solving ACOPF every 5-15 minutes [1], [2], and rapid demand fluctuations from Distributed Energy Resources (DERs) requiring even faster solution times, the computational burden of conventional solvers is becoming prohibitive [3], [4].

Although conventional solvers such as IPOPT may now be sped up by using the latest computing hardware [5], they are still too slow for near-real-time solutions and scale poorly to large grids. [6]. System operators, therefore, rely on relaxations [7], [8] and approximations such as DC Optimal Power Flow (DCOPF) [9], but these approximations are

always suboptimal with respect to ACOPF and are never AC-feasible [10]. Suboptimal solutions for ACOPF are particularly impactful, as even a 5% improvement in efficiency can lead to savings of billions of dollars and significantly reduced carbon emissions [1].

Machine learning can accelerate ACOPF by shifting the computational burden to offline training. Existing approaches comprise: (1) end-to-end learning, which directly predicts ACOPF variables [11]–[14] and (2) learning-to-optimize that accelerates conventional solvers through warm-starts [15], active constraint predictions [16] or ML-aided distributed optimization [17]. See [2] for a comprehensive taxonomy on ML for ACOPF. While these approaches offer varying degrees of speedups, important challenges remain regarding topology adaptability and scalability.

A key challenge is adaptability to topology changes from outages, maintenance or transmission switching. While Fully Connected Neural Networks (FNN) are the most widely used architecture in literature, they cannot adapt to topology changes [18]. Convolutional Neural Network (CNN) [19] and FNN variants [20] handle limited changes in system topology, but these remain grid-specific. Graph Neural Networks (GNNs) are the most naturally suited to handling topology variations [21], [22], but existing approaches combine GNN feature extraction with topology-specific fully connected layers, limiting their ability to handle arbitrary topology changes. Moreover, pure GNN approaches using local message passing struggle to accurately predict variables like voltage angle, which depend on global grid properties, leading to inferior performance compared to FNN baselines [18], [23].

Existing GNN approaches commonly use homogeneous graphs, treating all buses identically and modeling transmission lines as edges. Homogeneous graphs inadequately represent complex power networks where buses connect to varying numbers of generators, loads, and shunts. While [24] proposed a heterogeneous graph approach (CANOS), they require up to 60 GNN layers to propagate information through large networks, making training computationally expensive and scalability challenging. Furthermore, most works require retraining for each N-1 contingency or generating exhaustive N-1 training datasets, which becomes prohibitive for large grids.

In this work, we take important steps towards addressing the identified challenges. Inspired by [25], we propose a novel architecture for ACOPF. We summarize our main contributions as follows:

- 1) **GNN Architecture:** We propose a novel architecture combining heterogeneous GNN with a scalable transformer. Heterogeneous representation captures local information through explicit modeling of power system components, while the transformer efficiently accesses long-range information. The architecture is general and applies to power networks of any size.
- 2) **Zero-Shot Generalization:** We demonstrate generalization to arbitrary N-1 contingencies, showing adaptability to line or generator loss when trained only on default topology.
- 3) **Size Generalization:** We show favorable generalization across grid scales, with model pretrained on smaller grids improving performance on a larger grid.

We also open-source our implementation and baselines. The rest of the paper is organized as follows: Section II describes our approach. Section III presents case studies. Section IV discusses results and limitations, and Section V concludes the paper.

II. HYBRID HETEROGENEOUS MESSAGE PASSING NEURAL NETWORK

We propose a Hybrid Heterogeneous Message Passing Neural Network (HH-MPNN) for predicting ACOPF variables. MPNNs are a class of GNNs in which the model learns to make predictions on graphs through an iterative exchange of information between nodes, known as message passing. The proposed HH-MPNN consists of two components. 1) A heterogeneous MPNN which aggregates local information in the graph. 2) A scalable transformer that enables global information exchange through self-attention.

A. Heterogeneous Message Passing Neural Network

Our heterogeneous MPNN follows the encode-process-decode framework [26]. We represent the power grid with four node types (buses, generators, loads, shunts) and three edge types (transmission lines, transformers, and connector pseudo-edges linking buses to other node types). This explicit representation of power system components improves model expressivity compared to homogeneous graphs that treat all buses identically. The architecture operates in three stages: (1) **Encoding:** Project node and edge features into a shared embedding space, augmented with positional encodings (see section II-B). (2) **Processing:** Iteratively update node and edge embeddings through message passing with residual connections to prevent over-smoothing. (3) **Decoding:** Map final node embeddings to predicted ACOPF variables using type-specific decoders.

The encoding stage projects features through 2-layer multi-layer perceptrons (MLPs):

Codes will be made public after publication

$$h_{a,i}^0 = E_\theta^a(x_{a,i}) \oplus PE_i \quad (1a)$$

$$h_{e,i,j}^0 = E_\theta^e(e_{i,j}) \quad (1b)$$

where $a \in [N, G, S, L]$ denotes node type (bus, generator, shunt, load) and e denotes edge type (transmission line or transformer). $x_{i,j}$ and $e_{i,j}$ are input features, PE_i is the positional encoding and \oplus denotes concatenation. Message passing updates edges using adjacent node states, then aggregates edge messages to update nodes, both with residual connections:

$$\tilde{h}_{e,i,j}^k = U_\theta^e(h_{a,i}^{k-1}, h_{a,j}^{k-1} h_{e,i,j}^{k-1}) \quad (2a)$$

$$h_{e,i,j}^k = h_{e,i,j}^{k-1} + \tilde{h}_{e,i,j}^k \quad (2b)$$

$$m_{a,i}^k = \sum_{j \in N_i} (h_{e,i,j}^k) \quad (2c)$$

$$\tilde{h}_{a,i}^k = U_\theta^a(h_{a,i}^{k-1}, m_{a,i}^k) \quad (2d)$$

$$h_{a,i}^k = h_{a,i}^{k-1} + \tilde{h}_{a,i}^k \quad (2e)$$

All E_θ and U_θ functions are 2-layer MLPs with separate parameters for each node and edge type. For connector pseudo-edges, 1b is omitted, and edge updates in 2a use only adjacent node features without edge-specific parameters.

B. Transformer with Effective Resistance Positional Encoding

To capture long-range dependencies in power grids, we augment the local MPNN with a scalable transformer using performer attention [27], which approximates self-attention with linear complexity. Graph transformers require positional encodings to distinguish node positions. We use effective resistance, a domain-informed encoding that captures both local and global electrical distances [28].

Effective resistance represents the potential difference between a pair of nodes when a unit of current is injected into one node and leaves at the other [28]. Under DC approximation, the power balance equation can be written as $P = Q\theta$, where Q is the weighted Laplacian matrix with elements:

$$Q = \begin{cases} -B_{ij}, & i \neq j \\ \sum_{j=1}^N B_{ij}, & i = j \end{cases} \quad (3)$$

where B_{ij} is the susceptance of the edge connecting nodes i and j . From the DC power balance equation, θ can be written as Q^+P , where Q^+ is the pseudoinverse of Q . Effective resistance ω_{ij} can now be defined as [28]:

$$\omega_{ij} = (e_i - e_j)^T Q^+ (e_i - e_j) \quad (4)$$

where $\theta_i - \theta_j = \omega_{ij} P_{ij}$ and e_i, e_j are basic vectors with 1 at positions i, j respectively and 0 elsewhere.

The effective resistance matrix, $\Omega \in \mathbb{R}^{N \times N}$, gives a notion of how difficult it is to move a unit of current from node i to j , which considers all paths in the graph [29]. However, its dimensionality scales with grid size. To maintain a consistent

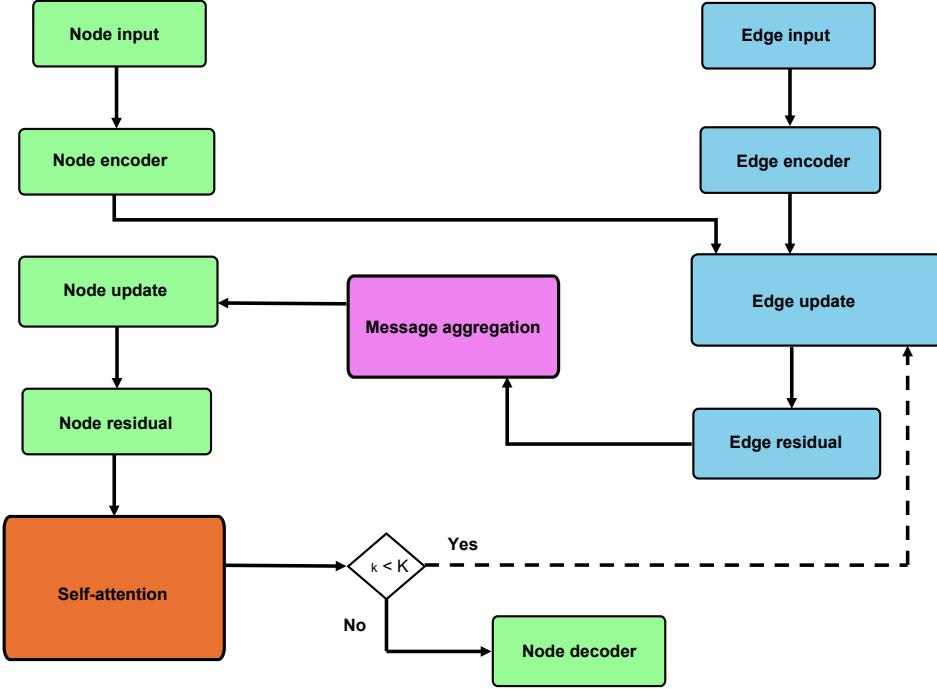


Fig. 1: The proposed HH-MPNN architecture with detailed message passing mechanism showing how information flows between different node and edge types. Skip connections and bidirectional updates enhance model expressivity. $K=5$ message passing layers are used.

dimension across different grids, we compute 5 statistical moments for each node's resistance vector:

$$PE_i = [min, max, std, median, mean].\Omega_{[:,i]} \quad (5)$$

This preserves distributional information about each node's electrical position while keeping the encoding dimension fixed at 5 across all grid sizes.

Fig. 1 shows the overall design and information flow within the proposed HH-MPNN. Our design significantly improves model expressiveness through explicit heterogeneous modeling of power system components and the combination of local and global information exchange, enabling effective learning even with a small number of message passing layers on large grids. Algorithm 1 summarises the complete HH-MPNN forward pass. After encoding node features with positional information in line 1, we alternate between local message passing (line 3) and global attention (line 5) for K layers. The attention mechanism operates on concatenated node embeddings from all types (line 4), enabling information exchange across the entire graph. We combine local MPNN updates with global transformer updates via element-wise addition (line 7), with a 2-layer MLP projection T_θ to integrate the representations. The transformer output also employs a residual connection (line 6). Type-specific 2-layer MLP decoders produce final predictions (line 9). We use $K=5$ message passing layers in all experiments.

Algorithm 1: Algorithm for HH-MPNN

```

1  $X^0 = E_\theta^a(X) \oplus PE$ 
2 for  $k = 0, 1, \dots, K - 1$  do
3    $(X_M^{k+1}, E^{k+1}) = \text{MPNN}(X^k, E^k)$ 
4   Aggregate node embeddings for all node types
5    $\hat{X}_T^{k+1} = \text{AT}(X^k)$ 
6    $X_T^{k+1} = X_T^k + \hat{X}_T^{k+1}$ 
7    $X^{k+1} = T_\theta(X_T^{k+1} + X_M^{k+1})$ 
8   Disaggregate node embeddings by node types
9  $Y = D_\theta^a(X^K)$ 

```

III. CASE STUDY

A. Dataset

We use OPFData dataset [30], the largest open-source ACOPF dataset available, containing 300,000 instances per grid. The dataset covers 10 grids from Power Grid Library [31]. Each dataset has two variants: 1) 'full topology' with default grid topology, where active and reactive loads vary independently by $\pm 20\%$ of nominal values. 2) 'N-1 topology' where each sample additionally has a randomly disconnected component (branch or generator). We use six grids from the dataset for our experiments: 14, 30, 57, 118, 500 and 2,000 buses. We refer to [30] for more details on how the data is generated and the data format.

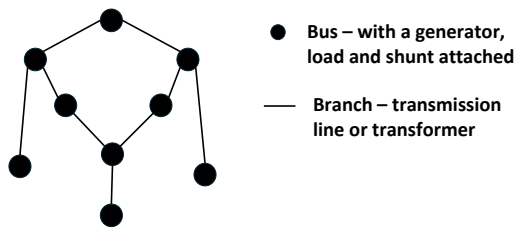
B. Baselines

We compare the performance of our proposed approach with the following baseline machine learning models:

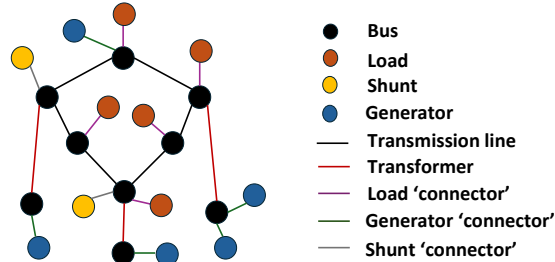
1) *Fully connected neural network (FNN)*: The network comprises 5 linear layers with a hidden dimension of 256 and ReLU activations. Input and output vectors are flattened, making the architecture tied to a specific grid topology.

2) *Convolutional neural network (CNN)*: We use 5 layers of 1D convolutions with ReLU activation and max pooling, followed by adaptive average pooling and a linear output layer with sigmoid activation. Like FNN, this architecture is topology-specific.

3) *Graph convolutional neural network (GCN)*: We represent buses as nodes and branches as edges, assuming uniform components at each bus (generator, load, shunt) and using generator masks to indicate presence/absence. This homogeneous representation is less flexible than our heterogeneous approach, as shown in Fig.2. The model comprises 5 graph convolution layers with a hidden dimension of 256. We apply GCN only to grids where homogeneous representation is tractable (14, 30, 57, 118 buses).



(a) Homogeneous representation of the power grid models transmission lines and transformers as the same. It is difficult to represent different numbers of components attached to each bus.



(b) Proposed heterogeneous graph with different node and edge types enables a more accurate representation of the power grid.

Fig. 2: Heterogeneous versus Homogeneous graph representation of the power grid

C. Experiment settings

We predict the voltage angles θ , voltage magnitude V , active generator power PG and reactive generator power QG . Following [6], we apply a sigmoid function to bound

System	Number of Parameters (10^5)			
	FNN	CNN	GCN	HH-MPNN
14-ieee	3.5	8.0	2.0	117.4
30-ieee	4.4	8.1	2.0	117.4
57-ieee	5.9	8.2	2.0	117.4
118-ieee	11.1	8.8	2.0	117.4
500-goc	35.4	11.3	—	117.4
2000-goc	135.4	19.4	—	117.4

TABLE I: Number of parameters for each ML model

outputs and satisfy inequality constraints (see Appendix A, 6b - 6d). Branch flows are computed using power flow equations (6g-6h). Angle difference 6e, branch thermal limit 6f, and power balance 6i constraints may be violated. We train the models with supervised mean square error (MSE) loss between predicted and ground truth variables. All models use Adam optimizer with learning rate 1×10^{-5} and weight decay 5×10^{-8} , trained for 100 epochs. We use 270,000 samples for training (90%), 15,000 for validation (5%) and 15,000 for testing (5%). Batch size is 256 for small grids (14-118 buses) and 16 for large grids (500-2,000 buses). All models have 5 layers with a hidden dimension of 256.

D. Model complexity

Table I compares model parameters across grids. FNN and CNN parameter counts increase with grid size due to topology-specific architectures. GCN parameters remain constant for the grids where we apply it (14-118 buses). HH-MPNN maintains constant parameters (117.4×10^5) across all grid sizes, demonstrating its flexibility. The larger parameter count also reflects the expressiveness of the heterogeneous graph and the transformer component.

E. Metrics

We evaluate models using three metrics: (1) **Mean Squared Error (MSE)** between predictions and ground truth for each ACOPF variable. (2) **Optimality gap**: percentage difference between model and ground truth objective costs. (3) **Constraint satisfaction**: average violations of constraints not strictly enforced (6e,6f,6i). Generator power and voltage magnitude constraints (6b - 6d) are satisfied by design through sigmoid activation. All violations are averaged over test datasets.

F. Prediction on 'full topology' dataset

Tables II-IV summarizes the results on the full topology dataset. **Prediction accuracy (Table II)**: HH-MPNN achieves the lowest MSE on most systems, but CNN performs best on the 118-bus grid. GCN shows an order of magnitude higher errors on small systems, though it achieves lower PG and QG errors on the 57-bus grid, potentially exploiting local generation patterns while struggling with voltage predictions. Model performance does not consistently degrade with grid size; for instance, both FNN and HH-MPNN show lower errors on the 2,000-bus grid compared to the 57-bus and 118-bus grids, suggesting that larger grids may have more regular power flow patterns. **Optimality gap (Table III)**: FNN, CNN, and HH-MPNN achieve negligible optimality gaps (< 1%) on all systems. CNN yields the lowest gaps

MSE ($\times 10^{-4}$)					
System	Model	θ	V	PG	QG
14-ieee	FNN	0.40	0.02	3.00	3.00
	CNN	0.03	0.02	0.08	2.00
	GCN	3.00	0.43	17.00	3.00
	HH-MPNN	0.01	0.00	0.21	0.06
30-ieee	FNN	0.32	0.06	13.00	3.00
	CNN	0.07	0.05	0.32	2.00
	GCN	2.00	0.60	3.00	0.98
	HH-MPNN	0.05	0.01	0.37	0.24
57-ieee	FNN	0.63	0.06	142.00	44.00
	CNN	0.64	0.06	139.00	44.00
	GCN	3.00	1.00	60.00	6.00
	HH-MPNN	0.37	0.02	106.00	20.00
118-ieee	FNN	2.00	0.10	55.00	75.00
	CNN	0.83	0.04	12.00	22.00
	GCN	9.00	0.77	318.00	68.00
	HH-MPNN	3.00	0.07	42.00	33.00
500-goc	FNN	3.00	0.05	13.00	11.00
	CNN	3.00	0.05	13.00	11.00
	HH-MPNN	1.00	0.03	6.00	7.00
2000-goc	FNN	0.88	0.09	10.00	17.00
	CNN	6.00	0.09	10.00	17.00
	HH-MPNN	0.34	0.06	5.00	9.00

TABLE II: Mean Squared Error (MSE) of the models on the full topology dataset. Errors are in pu except for θ in radians.

Average Constraint Violation ($\times 10^{-4}$)					
System	Model	$S_{ij}(+)$	$S_{ij}(-)$	Pb	Qb
14-ieee	FNN	0.00	0.00	5.60	0.56
	CNN	0.00	0.00	0.21	1.22
	GCN	0.00	0.00	8.08	40.13
	HH-MPNN	0.00	0.00	0.53	0.22
30-ieee	FNN	0.00	0.00	0.56	0.65
	CNN	4.42	0.05	0.14	1.14
	GCN	226.50	217.70	8.53	36.29
	HH-MPNN	0.25	0.00	0.19	0.62
57-ieee	FNN	0.00	0.00	1.68	0.46
	CNN	0.00	0.00	1.83	3.26
	GCN	0.00	0.00	4.08	4.73
	HH-MPNN	0.00	0.00	5.51	4.50
118-ieee	FNN	0.28	0.06	6.86	1.53
	CNN	1.57	1.18	0.15	5.60
	GCN	477.10	478.70	225.10	310.00
	HH-MPNN	11.12	11.35	3.04	13.75
500-goc	FNN	3.65	3.45	1.47	0.88
	CNN	0.00	0.00	1.18	2.34
	HH-MPNN	48.32	48.42	3.38	37.55
2000-goc	FNN	0.00	0.00	0.73	1.36
	CNN	0.00	0.00	1.26	8.48
	HH-MPNN	0.85	0.86	2.19	9.59

TABLE IV: Average constraint violations of the models on the full topology dataset. Violations are in pu.

System	Model optimality gap (%)			
	FNN	CNN	GCN	HH-MPNN
14-ieee	0.28	0.01	0.67	0.07
30-ieee	0.36	0.02	0.61	0.13
57-ieee	0.13	0.08	0.36	0.25
118-ieee	0.28	0.01	9.94	0.05
500-goc	0.05	0.04	N/A	0.17
2000-goc	0.02	0.01	N/A	0.01

TABLE III: Optimality gap of the models on the full topology dataset

overall. HH-MPNN achieves $< 0.1\%$ optimality gap on the 2,000-bus grid, demonstrating competitiveness for large-scale grids. **Constraint violations (Table IV):** All models satisfy angle difference constraints (θ_{ij}) completely. FNN and CNN show line flow violations ($S_{ij}(+)$ and $S_{ij}(-)$) on the order of 10^{-4} pu or zero. HH-MPNN has higher violations on 118-bus and 500-bus systems (10^{-3} pu). Power balance violations (Pb, Qb) are in the order of 10^{-4} pu for FNN/CNN and up to 10^{-3} pu for HH-MPNN. This is acceptable for approximate solvers and comparable to state-of-the-art results [6], [24].

G. Zero shot generalization to N-1 cases

A key property of graph-based models is adaptability to topology variations. We demonstrate zero-shot generalization whereby models trained only on full topology datasets (*mfull*) are applied to the test subset of the N-1 dataset without retraining. We compare this zero-shot experiment with models trained on the N-1 training subset (*mn1*) to establish an upper bound, which we refer to as the base experiment. The N-1 test subsets contain exponentially growing numbers of unique topologies with grid size. The 2,000-bus test set alone contains 2,513 unique topologies (see Appendix C, Figure 5). **Optimality gap (Figure 3):** HH-MPNN maintains stable performance across all systems, achieving $< 3\%$ optimality gap in zero-shot experiments despite training only on data with the full topology. Notably, performance on the largest system

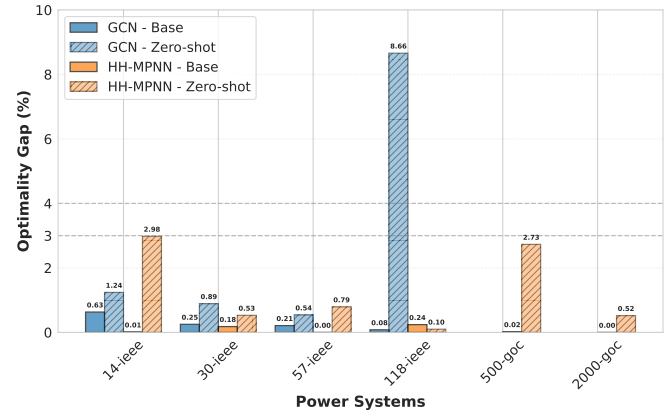


Fig. 3: Comparison of average optimality gaps in the base and zero-shot experiments. Optimality gaps for the proposed HH-MPNN remain below 3% when models trained on only the full topology are applied to numerous N-1 topologies.

(2,000-bus) is better than on the smallest (14-bus), which is consistent with larger grids being more robust to N-1 failures. GCN also exhibits good stability, except on the 118-bus system, where the zero-shot optimality gap reaches up to 8.7%. **Constraint violations (Table V):** Zero-shot experiments show larger violations than base experiments due to distribution shift between full topology (training) and N-1 topology (target) datasets. Despite this challenge, HH-MPNN maintains average violations below 0.1 pu in all cases. GCN shows higher violations (up to 0.15 pu for Pb). The zero-shot optimality gaps ($< 3\%$) are comparable to DCOPF approximations [24], demonstrating practical utility. Post-processing with power flow can further improve constraint satisfaction (see Appendix A for 118-bus results).

Average Constraint Violation ($\times 10^{-4}$)						
System	Model	θ_{ij}	$S_{ij}(+)$	$S_{ij}(-)$	Pb	Qb
14-ieee	GCN-B	0.00	0.00	0.00	15.02	17.81
	GCN-ZS	6.96	129.70	124.90	133.50	524.60
	HH-MPNN-B	0.00	0.00	0.00	0.02	2.70
	HH-MPNN-ZS	0.00	0.00	0.00	7.14	51.92
30-ieee	GCN-B	0.00	344.80	335.40	16.93	93.24
	GCN-ZS	6.09	702.50	697.40	99.60	361.90
	HH-MPNN-B	0.00	0.52	0.03	1.31	0.76
	HH-MPNN-ZS	0.00	8.57	6.51	1.35	32.46
57-ieee	GCN-B	0.00	0.00	0.00	9.07	0.47
	GCN-ZS	8.73	119.60	112.00	193.60	625.40
	HH-MPNN-B	0.00	0.00	0.00	2.10	12.11
	HH-MPNN-ZS	0.00	0.00	0.00	13.30	28.33
118-ieee	GCN-B	0.00	1244.00	1244.00	112.50	614.10
	GCN-ZS	0.45	1067.00	1063.00	97.57	735.30
	HH-MPNN-B	0.00	13.71	13.76	5.11	19.94
	HH-MPNN-ZS	0.00	290.60	288.40	46.67	102.20
500-goc	HH-MPNN-B	0.00	5.80	5.60	1.72	10.95
500-goc	HH-MPNN-ZS	0.00	114.70	114.80	38.03	38.04
2000-goc	HH-MPNN-B	0.00	0.28	0.28	1.03	2.65
2000-goc	HH-MPNN-ZS	0.00	5.33	5.37	6.23	55.59

TABLE V: Average constraint violations for GCN and HH-MPNN models in 'base' and 'zero-shot' experiments.

H. Analysing high impact contingencies

To understand the limits of zero-shot generalization, we examine high-impact contingencies leading to severe operational changes. We selected the top 40 costliest samples from each N-1 test subset. We then perform 3 experiments: (1) Naive baseline: applying the full-topology trained model (*mfull*), assuming default topology despite actual N-1 conditions, (2) Zero-shot: applying *mfull* with true N-1 topology information, and (3) Base: applying the N-1 trained model (*mn1*) with correct topology. Table VI quantifies the severity of the contingency cases in the 40 samples by comparing their mean objective costs to the full and N-1 topology training datasets' mean objective costs. Similar cost increases between the full topology training data (experiments 1 and 2) and the N-1 training data (experiment 3) reveal that the N-1 dataset is dominated by low-impact contingencies. For example, the 14-bus system shows about 48% cost increase for high-impact cases versus the training dataset mean, while larger systems show 3-15% increases. Fig. 4 shows the naive baseline yields optimality gaps of up to 26%, confirming these contingencies create significant challenges. Surprisingly, providing correct topology information to *mfull* (zero-shot) does not consistently improve performance. In several cases (57-bus, 118-bus, 500-bus), zero-shot performs worse than the naive baseline. This occurs because high-impact contingencies create operating conditions (generator dispatch levels, voltage angles) that lie outside *mfull*'s training distribution. Even with correct topology, the model must extrapolate beyond the training distribution, resulting in poor predictions. This explains why zero-shot generalization performs well on the complete N-1 test set (section III.G) but struggles on high-impact cases, as most contingencies do not significantly change the target distribution. (See Appendix B, Fig. 6, which illustrates this shift for voltage angles in the 118-bus system.

In contrast, *mn1* trained on N-1 data achieves optimality

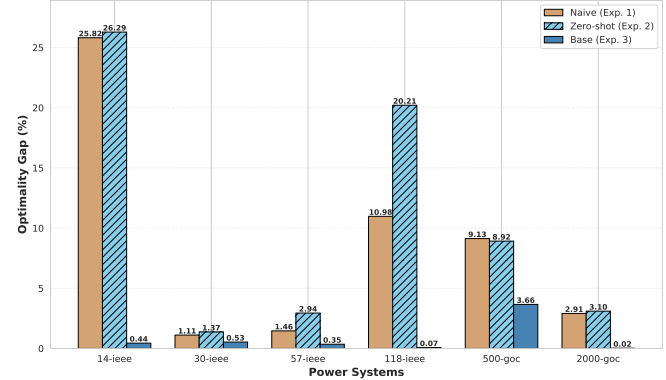


Fig. 4: Optimality gaps for high-impact N-1 contingencies. Naive: full-topology model assuming default topology. Zero-shot: full-topology model with correct N-1 topology. Base: model trained on N-1 data. Zero-shot sometimes performs worse than the naive baseline due to distribution shifts, while the N-1 trained model achieves <4% gaps across all systems.

gaps below 0.5% for all systems except 500-bus (3.66%), demonstrating that exposure to diverse topologies and their associated distribution ranges during training is essential for accurate high-impact contingency predictions. These results demonstrate that topology-aware architecture alone cannot overcome distribution shifts. For high-impact contingencies involving major generator disconnections or critical line outages, the model requires training distribution similar to the target distribution. The practical implication is that truly robust N-1 prediction requires training datasets spanning both topological diversity and the range of operating conditions expected during deployment, particularly for critical contingencies identified through security analysis [32].

System	Full topology dataset	N-1 dataset
14-ieee	48.13	44.81
30-ieee	11.04	11.53
57-ieee	12.37	12.22
118-ieee	15.10	14.60
500-goc	11.64	11.31
2000-goc	3.20	3.10

TABLE VI: Mean cost increase (%) from training set to high-impact test samples. Full topology dataset column: cost increase from full-topology training data (Exp 1 and 2) to high-impact N-1 test cases. N-1 dataset column: cost increase from N-1 training data (Exp 3) to the same cases. Similar values show that N-1 training data contains mostly low-impact contingencies.

I. Size generalization

Since HH-MPNN operates on graphs of arbitrary size, we investigate size generalization [33]: whether models can generalize to larger unseen grids. We train a model on combined N-1 datasets from smaller (14, 30, 57, 118, and 500-bus) grids (20,000 training samples per grid). We then test on the 2,000-bus grid in 3 experiments: (1) Training from scratch with only 3,000 training samples from the 2,000-bus grid (HH-MPNN-S). (2) Pretraining on smaller grids and testing on 15,000 testing samples of the 2000-bus grid with no finetuning. (HH-MPNN-WF). (3) Fine-tuning the pretrained model on the same 3,000 training samples (HH-MPNN-FT). Tables VII-VIII show that HH-MPNN-FT achieves lower MSE for all variables and

Model	Opt gap (%)	MSE ($\times 10^{-4}$)			
		θ	V	PG	QG
HH-MPNN-S	0.123	1.00	0.77	11.00	19.00
HH-MPNN-WF	5.840	1096.00	19.00	7466.00	1908.00
HH-MPNN-FT	0.003	0.98	0.61	6.00	17.00

TABLE VII: Average optimality gap and MSE comparison for the model trained from scratch (HH-MPNN-S), pretrained model without fine-tuning (HH-MPNN-WF) and pretrained model with fine-tuning (HH-MPNN-FT), on the 2,000-bus grid.

40 \times lower optimality gap (0.003% versus 0.123%) than HH-MPNN-S. HH-MPNN-WF leads to orders of magnitude worse predictions, showing the necessity of fine-tuning with a few samples from the target grid to learn scale-dependent features.

Violations ($\times 10^{-4}$)					
Model	θ_{ij}	$S_{ij}(+)$	$S_{ij}(-)$	P_b	Q_b
HH-MPNN-S	0.00	25.24	25.39	34.28	159.40
HH-MPNN-ZS	0.00	7635.00	7722.00	6963.00	31240.00
HH-MPNN-FT	0.00	37.08	37.61	38.35	166.30

TABLE VIII: Average constraint violations for the model trained from scratch (HH-MPNN-S), pretrained model without fine-tuning (HH-MPNN-WF) and pretrained model with fine-tuning (HH-MPNN-FT), on the 2,000-bus grid.

J. Analysing computational time

Table IX compares solution times between IPOPT and HH-MPNN. IPOPT time increases exponentially with grid size, making real-time solution impractical for large grids. HH-MPNN maintains nearly constant inference time (about 13ms) across all grid sizes, providing speedups of 10^3 to 10^4 compared to IPOPT. Beyond inference speedups, the graph-based approach reduces dataset generation costs. Zero-shot N-1 generalization eliminates the need to generate exhaustive N-1 training data, while generalization enables pre-training on smaller grids with cheaper data generation, reducing dataset requirements for new large systems. For example, the 3,000-sample fine-tuning dataset requires only 70 CPU hours to generate, compared to 6,300 CPU hours for the full 270,000-sample training set, demonstrating substantial computational savings.

IV. DISCUSSIONS

The proposed HH-MPNN provides accurate approximate ACOPF solutions across various grid sizes. For grids with fixed topology, our approach achieves performance comparable to FNN and CNN models while demonstrating the flexibility to handle N-1 topology changes that topology-specific architectures cannot. Our results challenge the assumption that graph-based models perform poorly when predicting generator setpoints and voltage angles. With sufficiently expressive architecture—combining heterogeneous graphs and transformers—both local and globally-dependent variables can be approximated accurately. We demonstrated topological flexibility through zero-shot prediction on N-1 variations and fine-tuning pretrained models on larger grids. We explore N-1

Average run time per instance ($\times 10^{-3}$ s)			
System	IPOPT	HH-MPNN	Average speed-up
14-ieee	33.2*	12.4	$\times 3$
30-ieee	102.3*	12.5	$\times 8$
57-ieee	328.8*	12.2	$\times 27$
118-ieee	420.7*	12.8	$\times 32$
500-goc	6486.0†	13.7	$\times 473$
2000-goc	83781.0†	14.7	$\times 5700$

TABLE IX: Average run time per instance comparing IPOPT and HH-MPNN, with computed average speed-up factors.

generalization limits, showing how distribution shifts affect model performance for high-impact contingency cases.

Limitations: We cannot guarantee satisfaction of all constraints. Average power balance violations reach 10^{-3} pu in some cases, which may require post-processing for strict AC feasibility. Our experiments used load variations and N-1 contingencies; extending to variable generator costs and other operational scenarios would strengthen generalization claims. Pre-computation of effective resistance matrices can be computationally intensive for large grids. Finally, future work should explore hybrid ML-optimization approaches for feasibility guarantees and rigorous theoretical analysis of generalization bounds.

V. CONCLUSION

We proposed a Hybrid Heterogeneous Message Passing Neural Network (HH-MPNN) for AC Optimal Power Flow that addresses topology adaptability and scalability challenges in existing machine learning approaches. By explicitly modeling power system components as distinct node and edge types combined with a scalable transformer, our architecture achieves $< 1\%$ optimality gaps on default topologies and $< 3\%$ gaps on zero-shot N-1 contingencies across grids from 14 to 2,000 buses. Pre-training on smaller grids improves performance on larger systems. Computational speedups of 10^3 to 10^4 compared to interior point solvers make the approach practical for real-time operations. These results demonstrate the potential for unified, generalizable graph-based models for diverse power system applications.

VI. ACKNOWLEDGEMENT

This research was funded by the Dutch Research Council, Veni Talent Program Grant 19161. We thank Ali Rajaei, Balthazar Donon, Jochen Stiasny, and Megha Khosla for insightful discussions during this work.

REFERENCES

- [1] M. B. Cain, R. P. O'Neill, and A. Castillo, “History of Optimal Power Flow and Formulations,” 2012.
- [2] H. Khaloie, M. Dolanyi, J.-F. Toubeau, and F. Vallée, “Review of Machine Learning Techniques for Optimal Power Flow,” *SSRN Electronic Journal*, 2024.
- [3] P. Panciatici, G. Bareux, and L. Wehenkel, “Operating in the Fog: Security Management Under Uncertainty,” *IEEE Power and Energy Magazine*, vol. 10, no. 5, pp. 40–49, Sep. 2012.

*IPOPT timing results from [34]

†IPOPT timing results from [24]

[4] H. F. Hamann, B. Gjorgiev, T. Brunschwiler, L. S. Martins, A. Puech, A. Varbella, J. Weiss, J. Bernabe-Moreno, A. B. Massé, S. L. Choi, I. Foster, B.-M. Hodge, R. Jain, K. Kim, V. Mai, F. Mirallès, M. De Montigny, O. Ramos-Leaños, H. Suprême, L. Xie, E.-N. S. Youssef, A. Zinfou, A. Belyi, R. J. Bessa, B. P. Bhattacharai, J. Schmude, and S. Sobolevsky, “Foundation models for the electric power grid,” *Joule*, vol. 8, no. 12, pp. 3245–3258, Dec. 2024.

[5] S. Shin, M. Anitescu, and F. Pacaud, “Accelerating optimal power flow with GPUs: SIMD abstraction of nonlinear programs and condensed-space interior-point methods,” *Electric Power Systems Research*, vol. 236, p. 110651, Nov. 2024.

[6] X. Pan, M. Chen, T. Zhao, and S. H. Low, “DeepOPF: A Feasibility-Optimized Deep Neural Network Approach for AC Optimal Power Flow Problems,” *IEEE Systems Journal*, vol. 17, no. 1, pp. 673–683, Mar. 2023.

[7] Z. Yang, H. Zhong, A. Bose, T. Zheng, Q. Xia, and C. Kang, “A Linearized OPF Model With Reactive Power and Voltage Magnitude: A Pathway to Improve the MW-Only DC OPF,” *IEEE Transactions on Power Systems*, vol. 33, no. 2, pp. 1734–1745, Mar. 2018, publisher: Institute of Electrical and Electronics Engineers (IEEE).

[8] D. K. Molzahn, J. T. Holzer, B. C. Lesieutre, and C. L. DeMarco, “Implementation of a Large-Scale Optimal Power Flow Solver Based on Semidefinite Programming,” *IEEE Transactions on Power Systems*, vol. 28, no. 4, pp. 3987–3998, Nov. 2013, publisher: Institute of Electrical and Electronics Engineers (IEEE).

[9] M. Chatzlos, F. Fioretto, T. W. K. Mak, and P. V. Hentenryck, “High-Fidelity Machine Learning Approximations of Large-Scale Optimal Power Flow,” Jun. 2020, arXiv:2006.16356 [eess].

[10] K. Baker, “Solutions of DC OPF are Never AC Feasible,” in *Proceedings of the Twelfth ACM International Conference on Future Energy Systems*. Virtual Event Italy: ACM, Jun. 2021, pp. 264–268.

[11] A. S. Zamzam and K. Baker, “Learning Optimal Solutions for Extremely Fast AC Optimal Power Flow,” in *2020 IEEE International Conference on Communications, Control, and Computing Technologies for Smart Grids (SmartGridComm)*. Tempe, AZ, USA: IEEE, Nov. 2020, pp. 1–6.

[12] S. Park, W. Chen, T. W. Mak, and P. Van Hentenryck, “Compact Optimization Learning for AC Optimal Power Flow,” *IEEE Transactions on Power Systems*, vol. 39, no. 2, pp. 4350–4359, Mar. 2024.

[13] W. Huang, M. Chen, and S. H. Low, “Unsupervised Learning for Solving AC Optimal Power Flows: Design, Analysis, and Experiment,” *IEEE Transactions on Power Systems*, vol. 39, no. 6, pp. 7102–7114, Nov. 2024.

[14] D. Owerko, F. Gama, and A. Ribeiro, “Unsupervised Optimal Power Flow Using Graph Neural Networks,” in *ICASSP 2024 - 2024 IEEE International Conference on Acoustics, Speech and Signal Processing (ICASSP)*. Seoul, Korea, Republic of: IEEE, Apr. 2024, pp. 6885–6889.

[15] K. Baker, “Learning Warm-Start Points for AC Optimal Power Flow,” May 2019, arXiv:1905.08860 [math].

[16] C. Crozier and K. Baker, “Data-driven Probabilistic Constraint Elimination for Accelerated Optimal Power Flow,” in *2022 IEEE Power & Energy Society General Meeting (PESGM)*. Denver, CO, USA: IEEE, Jul. 2022, pp. 1–5.

[17] M. Chatzlos, T. W. K. Mak, and P. V. Hentenryck, “Spatial Network Decomposition for Fast and Scalable AC-OPF Learning,” *IEEE Transactions on Power Systems*, vol. 37, no. 4, pp. 2601–2612, Jul. 2022.

[18] T. Falconer and L. Mones, “Leveraging Power Grid Topology in Machine Learning Assisted Optimal Power Flow,” *IEEE Transactions on Power Systems*, vol. 38, no. 3, pp. 2234–2246, May 2023.

[19] Y. Jia, X. Bai, L. Zheng, Z. Weng, and Y. Li, “ConvOPF-DOP: A Data-Driven Method for Solving AC-OPF Based on CNN Considering Different Operation Patterns,” *IEEE Transactions on Power Systems*, vol. 38, no. 1, pp. 853–860, Jan. 2023.

[20] M. Zhou, M. Chen, and S. H. Low, “DeepOPF-FT: One Deep Neural Network for Multiple AC-OPF Problems With Flexible Topology,” *IEEE Transactions on Power Systems*, vol. 38, no. 1, pp. 964–967, Jan. 2023.

[21] D. Owerko, F. Gama, and A. Ribeiro, “Optimal Power Flow Using Graph Neural Networks,” in *ICASSP 2020 - 2020 IEEE International Conference on Acoustics, Speech and Signal Processing (ICASSP)*. Barcelona, Spain: IEEE, May 2020, pp. 5930–5934.

[22] M. Gao, J. Yu, Z. Yang, and J. Zhao, “A Physics-Guided Graph Convolution Neural Network for Optimal Power Flow,” *IEEE Transactions on Power Systems*, vol. 39, no. 1, pp. 380–390, Jan. 2024.

[23] S. Liu, C. Wu, and H. Zhu, “Topology-Aware Graph Neural Networks for Learning Feasible and Adaptive AC-OPF Solutions,” *IEEE Transactions on Power Systems*, vol. 38, no. 6, pp. 5660–5670, Nov. 2023.

[24] L. Piloto, S. Liguori, S. Madjiheurem, M. Zgubic, S. Lovett, H. Tomlinson, S. Elster, C. Apps, and S. Witherspoon, “CANOS: A Fast and Scalable Neural AC-OPF Solver Robust To N-1 Perturbations,” Mar. 2024, arXiv:2403.17660 [cs].

[25] L. Rampášek, M. Galkin, V. P. Dwivedi, A. T. Luu, G. Wolf, and D. Beaini, “Recipe for a General, Powerful, Scalable Graph Transformer,” Jan. 2023, arXiv:2205.12454 [cs].

[26] P. W. Battaglia, R. Pascanu, M. Lai, D. Rezende, and K. Kavukcuoglu, “Interaction Networks for Learning about Objects, Relations and Physics,” Dec. 2016, arXiv:1612.00222 [cs].

[27] K. Choromanski, V. Likhoshesterov, D. Dohan, X. Song, A. Gane, T. Sarlos, P. Hawkins, J. Davis, A. Mohiuddin, L. Kaiser, D. Belanger, L. Colwell, and A. Weller, “Rethinking Attention with Performers,” Nov. 2022, arXiv:2009.14794 [cs].

[28] H. Cetinay, F. A. Kuipers, and P. Van Mieghem, “A Topological Investigation of Power Flow,” *IEEE Systems Journal*, vol. 12, no. 3, pp. 2524–2532, Sep. 2018.

[29] Y. Koç, M. Warnier, P. V. Mieghem, R. E. Kooij, and F. M. Brazier, “The impact of the topology on cascading failures in a power grid model,” *Physica A: Statistical Mechanics and its Applications*, vol. 402, pp. 169–179, May 2014.

[30] S. Lovett, M. Zgubic, S. Liguori, S. Madjiheurem, H. Tomlinson, S. Elster, C. Apps, S. Witherspoon, and L. Piloto, “OPFData: Large-scale datasets for AC optimal power flow with topological perturbations.”

[31] S. Babaeinejad sarookolaei, A. Birchfield, R. D. Christie, C. Coffrin, C. DeMarco, R. Diao, M. Ferris, S. Fliscounakis, S. Greene, R. Huang, C. Josz, R. Korab, B. Lesieutre, J. Maeght, T. W. K. Mak, D. K. Molzahn, T. J. Overbye, P. Panciatici, B. Park, J. Snodgrass, A. Tbaileh, P. V. Hentenryck, and R. Zimmerman, “The Power Grid Library for Benchmarking AC Optimal Power Flow Algorithms,” Jan. 2021, arXiv:1908.02788 [math].

[32] O. Arowolo, J. Stiasny, and J. Cremer, “Exploring extrapolation of machine learning models for power system time domain simulation,” *Sustainable Energy, Grids and Networks*, vol. 43, p. 101908, Sep. 2025.

[33] G. Yehudai, E. Fetaya, E. Meirom, G. Chechik, and H. Maron, “From Local Structures to Size Generalization in Graph Neural Networks,” Jul. 2021, arXiv:2010.08853 [cs].

[34] F. Fioretto, T. W. K. Mak, and P. V. Hentenryck, “Predicting AC Optimal Power Flows: Combining Deep Learning and Lagrangian Dual Methods,” Dec. 2019, arXiv:1909.10461 [eess].

APPENDIX A PROBLEM FORMULATION

For a power system with N buses, \mathcal{E} branches, G generators, L loads and S shunts, the ACOPF problem is defined as follows:

$$\min \sum_{i \in G} a(PG_i^2) + b(PG_i) + c \quad (6a)$$

s.t.

$$PG_i^{\min} \leq PG_i \leq PG_i^{\max} \quad \forall i \in G \quad (6b)$$

$$QG_i^{\min} \leq QG_i \leq QG_i^{\max} \quad \forall i \in G \quad (6c)$$

$$V_i^{\min} \leq V_i \leq V_i^{\max} \quad \forall i \in N \quad (6d)$$

$$\theta_{ij}^{\min} \leq \theta_{ij} \leq \theta_{ij}^{\max} \quad \forall (i, j) \in \mathcal{E} \quad (6e)$$

$$|S_{ij}| \leq S_{ij}^{\max} \quad \forall (i, j) \in \mathcal{E} \quad (6f)$$

$$S_{ij} = (Y_{ij} + Y_{ij}^c)^* \cdot \frac{|V_i|^2}{|T_{ij}|^2} - Y_{ij}^* \frac{V_i V_j^*}{T_{ij}} \quad \forall (i, j) \in \mathcal{E} \quad (6g)$$

$$S_{ji} = (Y_{ij} + Y_{ij}^c)^* \cdot |V_j|^2 - Y_{ij}^* \frac{V_i^* V_j}{T_{ij}^*} \quad \forall (i, j) \in \mathcal{E} \quad (6h)$$

$$\sum_{k \in G} SG_k - \sum_{k \in L} SL_k - \sum_{k \in S} SS_k = \sum_{(i, j) \in \mathcal{E}} S_{ij} \quad \forall i \in N \quad (6i)$$

Here, a , b and c are the quadratic, linear and constant cost coefficients of generators, respectively. PG_i and QG_i are the generators' active and reactive powers, respectively. V_i is the voltage magnitude at a bus i , while θ_{ij} is the voltage angle difference between buses i and j respectively. S_{ij} is the complex power over branch (i, j) , in the forward direction, S_{ji} in the complex branch power in reverse direction. SG_k is the complex power of generator k , SL_k is the complex power at load k and SS_k is the complex power at shunt k . Y_{ij} is the admittance of a branch, Y_{ij}^c is the charging admittance of the branch while T_{ij} is the complex transformation ratio of the branch.

6a is the objective cost to be minimized. 6b and 6c are the active and reactive generator power limits, respectively. 6d is the voltage magnitude limit at a bus. 6e is the angle difference limit between two buses. 6f is the branch thermal limit. 6g and 6h are the branch flow equations. 6i is the power balance equation and ensures the sum of power into a bus is equal to the sum of power out of it, as specified by Kirchhoff's law.

APPENDIX B

POST PROCESSING MODEL PREDICTIONS WITH POWER FLOW

Power flow can be used to process the predictions from the ML models further, to ensure satisfaction of power balance constraints and make the obtained solution AC-feasible. However, we note that correcting the model predictions with power flows may now lead to violations of inequality constraints, such as voltage and power bounds. In the power flow formulation, only the slack bus has its active generation adjusted. This can lead to a violation of active power bound at the slack bus. Generations at other PV buses remain the same as predicted by the ML model. The reactive generation at PQ buses may be changed. We do not enforce reactive power limits; however, this can be achieved by converting PV buses to PQ buses at the reactive power limit. Table X shows the change in optimality, while Table XI shows the constraint violations for each model after power flow postprocessing on the 118-bus grid.

Optimality gap (%)		
Model	Before PF	After PF
FNN	0.28	0.06
CNN	0.01	0.04
GCN	9.94	2.03
HH-MPNN	0.05	0.09

TABLE X: Optimality gap of the models before and after power flow post-processing on 118-bus grid.

Model	Average Constraint Violation ($\times 10^{-4}$)					
	$S_{ij}(+)$	$S_{ij}(-)$	PG	PQ	Pb	Qb
FNN	2.03	1.95	0.00	193.60	0.0220	617.40
CNN	2.00	1.61	0.00	196.60	0.0001	615.30
GCN	32.57	37.22	0.00	846.80	0.0005	403.00
HH-MPNN	0.25	0.94	0.00	1308.00	0.0006	596.60

TABLE XI: Constraint violations after power flow post-processing on 118-bus grid. PG and PQ are the active and reactive power bounds violations. Other violable constraints have zero violations.

APPENDIX C SUPPORTING FIGURES

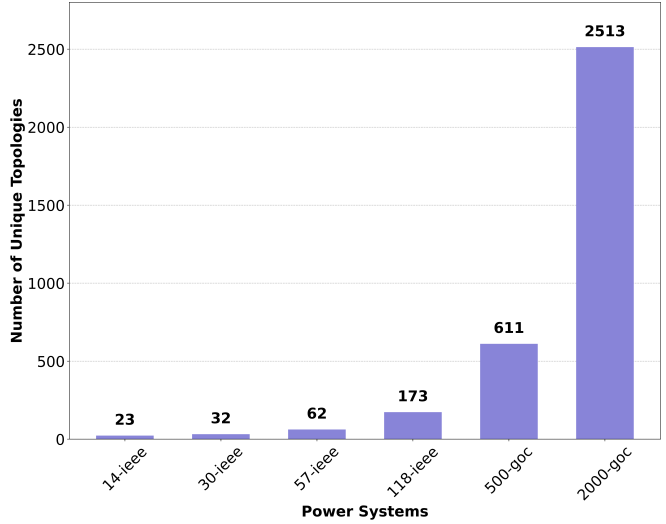


Fig. 5: Each bar shows the number of unique topologies in the N-1 test subset for each grid. There is exponential growth in the number of grid topologies with increasing grid size.

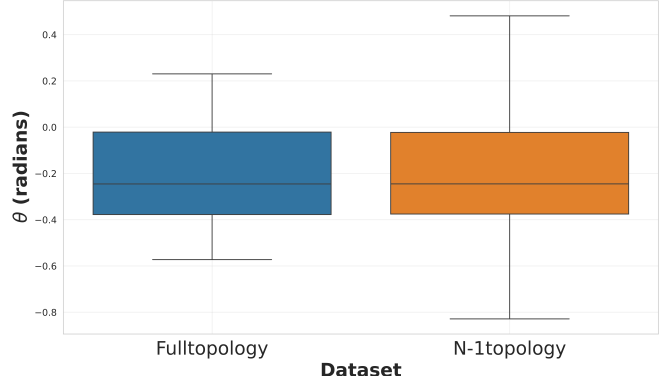


Fig. 6: Distribution of voltage angles in the full topology and N-1 topology datasets for the 118-bus system